Experimental assessment of the stress-sensitivity of combined elastic and electrical anisotropy in shallow reservoir sandstones

By

Ismael Himar Falcon-Suarez[1*]

North Laurence[1]

Ben Callow[1,2]

Gaye Bayrakci[1]

Jon Bull[1,2]

&

Angus Best[1]

(1) National Oceanography Centre, University of Southampton Waterfront Campus. European Way, SO14 3ZH, Southampton, United Kingdom.

(2) University of Southampton, National Oceanography Centre Southampton, Southampton, SO14 3ZH, UK

[*]Corresponding author: National Oceanography Centre, University of Southampton Waterfront Campus. European Way, SO14 3ZH, Southampton.

Phone: +44 (0)23 8059 6666 Office: 786/15 e-mail: isfalc@noc.ac.uk

ABSTRACT

Seismic and electromagnetic properties are generally anisotropic, depending on the microscale rock fabric and the macroscale stress field. Here, we assess stress-dependent anisotropy of poorly consolidated (porosity ~0.35) sandstones (broadly representative of shallow reservoirs) experimentally, combining ultrasonic (0.6 MHz P-wave velocity, V_P, and attenuation, $1/Q_P$) and electrical resistivity measurements. We used three cores from an outcrop sandstone sample extracted at 0º, 45º and 90º angles with respect to the visible geological bedding plane, and subjected them to unloading/loading cycles with variations of the confining (20 – 35 MPa) and pore (2 – 17 MPa) pressures. Our results indicate that stress field orientation, loading history, rock fabric and the measurement scale, all affect the elastic and electrical anisotropies. Strong linear correlations ($R^2 > 0.9$) between V_P, $1/Q_P$ and resistivity in the three considered directions suggest that the stress orientation similarly affects the elastic and electrical properties of poorly consolidated, high porosity (shallow) sandstone reservoirs. However, resistivity is more sensitive to pore pressure changes (effective stress coefficients $n > 1$), while P-wave properties provide simultaneous information about the confining (from V_P, with n slightly below 1) and pore pressure (from $1/Q_P$, with n slightly above 1) variations. We found n is also anisotropic for the three measured properties, as a more intense and rapid grain rearrangement occur when the stress field changes result from oblique stress orientations with respect to rock layering. Altogether, our results highlight the potential of joint elastic-electrical stress-dependent anisotropy assessments to enhance the geomechanical interpretation of reservoirs during production or injection activities.

INTRODUCTION

Anisotropic properties of marine sediments provide information about the porous network and the deformation patterns of the geological complex. The characterization of the pore structures controlling preferential fluid migration pathways is essential for estimating reservoir sealing efficiency and geomechanical integrity during production or injection activities, relevant for oil and gas and carbon dioxide (CO_2) storage (safe long-term disposal) industries (Jansen et al., 2019; Rutqvist, 2012).

Seismic and electromagnetic surveys are the most extensive field-scale monitoring techniques for reservoir interpretation. The combination of compressional (P-) waves an electrical resistivity data is particularly useful for under seabed exploration surveys, where shear (S-) wave collection is limited by the commonly encountered low amplitude of S-waves in marine wide-angle seismic data.

The bulk electrical resistivity of sedimentary rocks depends on the porosity, pore size distribution and connectivity, the electrical resistivity of the saturating fluid(s) and, to a lesser extent, the electrical properties of the mineral fraction. Therefore, in a saturated porous medium, the electrical resistivity anisotropy can be used as a proxy of the flow patterns (e.g., Nabawy et al., 2010) to develop reservoir-scale fluid flow models for pore fluid pressure and fault stability predictions. Characterizing the electrical anisotropy of defined geological contexts is of great importance for enhancing the development of numerical models to improve structural reservoir interpretation (North et al., 2013). However, in complex deformed media, fluid flow models commonly neglect the microstructural-induced permeability anisotropy (Farrell et al., 2014); here, seismic anisotropy is crucial to reconstruct the structure and the hydrodynamics of the geological complex. Despite this fact, very

little work has been conducted to study combined electrical and elastic data at the microscale, essential to better interpret larger-scale phenomena.

Granular sedimentary rocks are mainly formed in marine environments and therefore have an inherent degree of anisotropy due to preferred grains orientation during deposition and compaction (i.e., either anisotropic minerals or isotropic minerals with particular elongated shapes (Thomsen, 1986)). Thereafter, the sediments are exposed to deformation processes, developing a secondary form of anisotropy related to stress-induced cracks and fractures and, at larger scale, the layering of the sedimentary complex. Despite being formed by anisotropic components (minerals), the sedimentary rocks are only weakly anisotropic in most cases (Thomsen, 1986).

In general, when the rock is deformed, any considered anisotropy varies in distribution and intensity with the scale of observation. Field-scale resistivity data are conditioned by both the rock fabric (microstructure) and regional bedding (10s to 100s meters) scale (North et al., 2013). Then, when electric and elastic properties are available, the comparison between different scale fabrics is of great interest to distinguish between fluid dynamics (resistivity) and deformation patterns (waves). A number of works have addressed the integration of elastic waves and resistivity properties of rock samples under reservoir conditions, at the laboratory (centimetric) scale. They include general characterizations of common (sandstones and carbonates) reservoir formations (Louis et al., 2003, 2004; Wang et al., 2009; Wang and Gelius, 2010; Han et al., 2011a, b, 2018; Falcon-Suarez et al., 2019), pore fluid distribution monitoring during CO_2 geosequestration (Alemu et al., 2013; Falcon-Suarez et al., 2016, 2017b, 2018; Nooraiepour et al., 2018), methane hydrate formation (Sahoo et al., 2018; Attias et al., 2020) and the assessment of secondary

(alteration) mineralization (e.g., the degree of serpentinization of mafic/ultramafic rocks (Falcon-Suarez et al., 2017c; Bayrakci et al., 2018)). Commonly, these studies assess the stress dependency of both parameters under defined states of stress and pore fluid conditions. But, more complicated is the analysis of their variation with the orientation (i.e., anisotropy), which is likewise crucial for understanding most of the geological contexts.

Historically, the elastic anisotropy of rock formations has been addressed by the propagation properties of elastic waves along different directions on core plugs, to obtain the full stiffness tensor (e.g., Wang, 2002). Then, the anisotropy of transverse isotropic (TI) media (the most common case in nature) is straightforward determined from the obtained velocities by applying the three dimensionless parameters introduced by Thomsen (1986) (e.g., Rathore et al., 1995; Wang, 2002 Best et al., 2007; Martínez and Schmitt, 2013; Tillotson et al., 2014; Falcon-Suarez et al., 2017a). In this regard, we find experimental approaches based on multidirectional array measurement using a single core plug (e.g., Wang, 2002; Kovalyshen et al., 2018), and several cores extracted at different angles (with respect to the formation bedding) from the same rock (e.g., Louis et al., 2004; Best et al., 2007; Martínez and Schmitt, 2013; Falcon-Suarez et al., 2017a). For resistivity anisotropy determinations, we also find the single-core (Guo et al., 2011; North et al., 2013; North and Best, 2014; Falcon-Suarez et al., 2017c, 2019; Bayrakci et al., 2018; Nooraiepour et al., 2018) and multi-coring (e.g., Wang et al., 2009; Falcon-Suarez et al., 2017a) experimental strategies. The use of several plugs implies relying the uniformity of adjacent plugs is preserved (i.e., absolute homogeneity of precursor specimen), which in practice is impossible to guarantee (Best et al., 2007);

but, unlike the single-core, this method is easily implemented using conventional equipment.

Many studies have addressed the anisotropy of rocks based on their elastic or electrical properties. However, the simultaneous assessment of both anisotropic properties of rocks is probably limited to the data reported by Han (2018). This combined approximation is essential to understand the interplay of the anisotropy sources involved in a sedimentary deformational process and to develop new joint elastic-electrical theoretical models (Carcione et al., 2007). Furthermore, elastic and electrical properties show different stress dependency. The former group is more sensitive to changes in compliant porosity, which is the porosity fraction associated with the microcracks and grain vicinities that rapidly close upon increasing loading; while the latter is to the stiff porosity, which refers to the equidimensional voids fraction frequently addressed as pores (Shapiro et al., 2015). The total porosity is the sum of the stiff and compliant porosity fractions (Kaselow and Shapiro, 2004). Therefore, the combined assessment of elastic and electrical anisotropy properties of rocks must be framed within a stress history context. This information is needed to confirm the possibility of using field geophysical anisotropy surveys (both seismic and electromagnetic) for linking the opening or closing, and preferred directions, of sub-surface fluid flow pathways to the geomechanical response to geo-pressure changes of reservoir rocks during production/injection activities.

In this contribution, we present a well-controlled laboratory experiment to unambiguously link the anisotropy of P-wave velocity and attenuation, and resistivity of a clean, strongly bedded quartz sandstone, and their dependency to pore and confining pressure. The different properties were measured in three plugs cored at 0°, 45° and 90° with respect to the bedding plane, from a (weakly cemented)

sandstone specimen with visual lamination (anisotropy) over a range of stress conditions, including loading and unloading cycles. We evaluated the stress dependency of the rock anisotropy as measured through hand specimen (centimeter) and microstructure scales (i.e., rock fabric versus sample fabric), using both the single-core and multicore techniques.

MATERIALS AND METHODS

Rock samples

Three core plugs were extracted from a poorly consolidated sandstone specimen at 0°, 45° and 90°, with respect to the lamination plane (Figure 1). We denoted the samples as S-0, S-45 and S-90, for coring parallel, oblique and vertical with respect to the vertical axis to lamination (i.e., transverse isotropy with an orthogonal axis of rotational symmetry). The samples were ~2 cm length (S-0 slightly shorter), ~4.7 cm diameter each, with porosity ϕ ~0.35 (by He-pycnometry) and dry density 1440 ±15 kg/m^3. The X-ray diffraction (XRD) analysis (conducted with a PhilipsX'Pert pro XRD – Cu X-ray tube) revealed the rock is formed by ~62% quartz, ~35% albite and ~3% illite.

The precursor specimen was collected from the Yellowbank Creek Sandstone Injectite Complex (YCIC), located along Panther Beach, Santa Cruz, California. The YCIC formed from complex sediment fluidisation and remobilisation process in the shallow surface (Scott et al., 2009). The horizontal laminations have been interpreted to form as a result of post-fluidisation compaction and lateral shearing during horizontal intrusion of sediment within the shallow surface. The rock was cohesive enough to allow coring and sample preparation protocols for laboratory tests, and

therefore an ideal candidate to investigate anisotropic properties of shallow granular sedimentary formations.

Experimental procedure

The test was conducted using the high-pressure room-temperature (20º C) experimental setup for (multi-) flow-through tests at the National Oceanography Centre, Southampton (NOCS). The rig allows geophysical signatures (ultrasonic waves and resistivity) of rock samples to be related to their hydromechanical changes during the injection of different pore fluids (e.g., Falcon-Suarez et al., 2017b). For this experiment, we have adopted a monophasic pore fluid configuration using a 3.5% NaCl synthetic brine solution.

The experiment was configured to investigate changes in the ultrasonic and electrical properties of the three samples under variable state of stress conditions. Because confining and pore pressure may affect differently the measured property (i.e., different effective stress coefficients; Falcon-Suarez et al. (2019)), a geological uplift process was simulated using loading/unloading confining stress (P_c) paths and increasing pore pressure (P_p) from one path to the next. The stress path covered the six P_c steps 20-25-30-35-30-20 MPa, repeated four times varying P_p as 2-7-12-17 MPa (21 states of stress in total because the first P_c path started at 35 MPa; see the sequence sorted in Table 1). To ensure the sample was in equilibrium before measuring the geophysical parameters, we applied a gentle loading/unloading stress rate of ~0.05 MPa/s, while keeping constant either the pore pressure or the confining stress depending on the step of the state of stress sequence, and then waited ~30 min after each target state of stress was reached.

Experimental rig

The rig is configured around a triaxial cell core holder designed to host 5 cm diameter, 2 cm length core plugs, up to 60 MPa of confining and pore pressure (Figure 2). Both the confining and pore pressure are controlled by dual ISCO EX-100D systems. Axial and radial confining stress (σ_1 and $\sigma_2 = \sigma_3$, respectively) can be independently applied to the triaxial vessel. For this experiment, we used a deviatoric stress (i.e., $\sigma_1 - \sigma_3$) of 0.5 MPa, so that $P_c = (\sigma_1 + 2\sigma_3)/3$, to force a weak preferential stress along the axial direction. Pore fluid is delivered/received using fluid transfer vessels (FTVs) to minimize fluid-induced corrosiveness effects on the equipment. For this experiment, a FTV is used for delivering the (3.5% NaCl) synthetic brine upstream, while another FTV is used for receiving the pore fluid downstream. Here we introduce the essential information regarding the ultrasonic and electrical resistivity equipment; for further details about multi-flow configurations and hydromechanical instrumentation we refer to Falcon-Suarez et al. (2017b).

Geophysical measurements

The rubber sleeve isolating the rock sample from the confining mineral oil inside the vessel is equipped with an array of 16 stainless steel electrodes (two rings of eight electrodes) connected to an electrical resistivity tomography data acquisition system designed and developed at the NOC (North et al., 2013). Using a tetra-polar electrode configuration, each run collects 208 individual (tetra-polar) measurements, which are then inverted using a variation of the software EIDORS (Andy & William 2006) MATLAB toolkit. For processing our data, we used the parameters and configuration described in Falcon-Suarez et al. (2017c). Under our operating conditions, the bulk electrical resistivity error is <1% (i.e., bulk resistivity <100 Ω m at

frequencies 1-500 Hz). But, the anisotropic inversion to infer the main components of resistivity increases the error up to ~5%.

The sample is axially confined with two platens housing ultrasonic pulse-echo sensors. The core plug is isolated from the rest of the rig and the ultrasonic transducer by two polyether ether ketone (PEEK) buffer rods of well-defined acoustic impedance and low energy loss. The PEEK provides a reliable delay path to enable the identification of top/base sample reflections for calculating ultrasonic P- and S-wave velocities and attenuations using the pulse-echo technique (Best, 1992). The technique provides useable frequencies between 300 - 1000 kHz. Within this range, the velocity precision is ± 0.1% and the accuracy is ± 0.3% (95% confidence), while the attenuation accuracy is ± 0.1 dB/cm (Best, 1992). For this test, we processed the ultrasonic data to compare the elastic properties of our three samples at a single (ultrasonic) frequency of 600 kHz, obtained from Fourier analysis of broad band signals. We used a dual P-S-wave transducer in one platen and a single S-wave transducer in the opposite one.

Anisotropy determinations

Ultrasonic P-wave velocity (V_P) and attenuation ($1/Q_P$) were measured together with electrical resistivity for each state of stress for samples S-0, S-45 and S-90. Additionally, we collected two orthogonal components of S-wave velocity (V_{S1} and V_{S2}) and attenuation ($1/Q_{S1}$ and $1/Q_{S2}$) for S-90 only, to complete the anisotropy assessment (i.e., transverse isotropy with a vertical axis of rotational symmetry, VTI) using Thomsen's parameters (Thomsen, 1986; Wang, 2002; Louis et al., 2004; Zhu and Tsvankin, 2006; Chichinina et al., 2009; Martínez and Schmitt, 2013). For this, the ultrasonic transducers were orthogonally faced to simultaneously provide with maximum and minimum S-wave amplitudes, corresponding to S-wave polarization at

0° and 90° to the bedding plane in S-90. However, because some S-wave signals were weak below 13 MPa of differential pressure ($P_{diff} = P_c - P_p$), we limit our ultrasonic anisotropy assessment to the P_{diff} range 13-33 MPa.

Here, we only present the simplified equations from which we obtain the three Thomsen's parameters, for both the velocities and attenuation. For further details about the elastic tensor theory we refer to Thomsen (1986) for velocity, Zhu and Tsvankin (2006) and Chichinina et al. (2009) for the attenuation, and Louis et al. (2004) for any measured property. Thus, first we obtain the five elastic constants of the material from measured ultrasonic P-wave velocity and attenuation (with subscripts 0, 45 and 90 for wave propagating parallel, at 45°, and perpendicular to the vertical axis to lamination, respectively) and densities (ρ), as follows:

$$c_{11} = \rho V_{P(0)}^2 , \; Q_{11} = Q_{P(90)} , \qquad (1, 2)$$

$$c_{33} = \rho V_{P(90)}^2 , \; Q_{33} = Q_{P(0)} , \qquad (3, 4)$$

$$c_{55} = \rho V_{S(90)}^2 , \; Q_{55} = Q_{S(0)} , \qquad (5, 6)$$

$$c_{66} = \rho V_{S(0)}^2 , \; Q_{66} = Q_{S(90)} \qquad (7, 8)$$

and

$$c_{13} = \left[\left(4\rho V_{P(45)}^2 - c_{11} - c_{33} - 2c_{55} \right)^2 - \left(c_{11} - c_{33} \right) \right]^{0.5} - c_{55} , \qquad (9)$$

$$Q_{13} = Q_{33} \frac{c_{33} - 2c_{55}}{c_{33} - 2c_{55} \dfrac{Q_{33}}{Q_{55}}} . \qquad (10)$$

Then, the Thomsen's parameters are derived from the elastic constants for velocities and attenuation:

$$\varepsilon = \frac{c_{11} - c_{33}}{2c_{33}} , \; \varepsilon_Q = \frac{Q_{P(90)}^{-1} - Q_{P(0)}^{-1}}{Q_{P(0)}^{-1}} , \qquad (11, 12)$$

$$\gamma = \frac{c_{66} - c_{55}}{2c_{55}}, \quad \gamma_Q = \frac{Q_{S(90)}^{-1} - Q_{S(0)}^{-1}}{Q_{S(0)}^{-1}}, \qquad (13, 14)$$

and

$$\delta = \frac{\left(c_{13} + c_{55}\right)^2 - \left(c_{33} - c_{55}\right)^2}{2c_{33}\left(c_{33} - c_{55}\right)}, \quad \delta_Q = 4\frac{Q_{33} - Q_{55}}{Q_{55}}\frac{c_{55}}{c_{33}} + 2\frac{Q_{33} - Q_{13}}{Q_{13}}\left(1 + 2\delta - 2\frac{c_{55}}{c_{33}}\right). \qquad (15, 16)$$

From the expressions above, the P-wave phase velocity and attenuation for weakly anisotropic VTI elastic media can be obtained as follows:

$$V_P^2(\theta) = V_{P(90)}^2\left(1 + 2\delta\sin^2\theta\cos^2\theta + 2\varepsilon\sin^4\theta\right) \qquad (17)$$

and

$$1/Q_P(\theta) = 1/Q_{P(90)}\left(1 + \delta_Q\sin^2\theta + \left(\varepsilon_Q - \delta_Q\right)\sin^4\theta\right). \qquad (18)$$

Electrical resistivity anisotropy was initially calculated based on Nabawy et al. (2010), through the ratio of the maximum and minimum bulk resistivity (R_{max} and R_{min}) as:

$$\lambda_E = \left(\frac{R_{\max}}{R_{\min}}\right)^{0.5}. \qquad (19)$$

For completeness, we also calculated the intermediate resistivity (R_{int}) anisotropy λ_e from the relationship between the higher and intermedium values, by substituting R_{min} by R_{int} in the expression above. Next, we investigated the resistivity anisotropy of each sample using the technique described in North et al. (2013), which enables the assessment of both the electrical heterogeneity and anisotropy of rock samples (EHAR) from single cores. The EHAR technique system was assessed by North and Best (2014), who performed anisotropic inversion sensitivity tests in a number of sandstones. We use the EHAR technique to analyze the effect of the scale (from visual hand-scale to grain-scale features) on the resistivity.

Petrographic analysis

After the test, vertical thin sections (containing the true dip plane) were manufactured from each sample (Figure 1b). The thin sections were analyzed under a standard petrographic microscope coupled to high-resolution camera. The images acquired during the petrographic analysis were used to estimate the preferential elongation and distribution of the porosity fraction using ImageJ software. First, grain boundaries were detected by the Sobel edge detection algorithm of the GNU Image Manipulation Program software (Kylander and Kylander, 1999). Then, the high-resolution, colored-thin section images were visualized in Lab color space, dimensioning lightness and two-color component (green-red, and blue-yellow) factors (Lakio et al., 2010). The lightness component was used for edge detection, after applying a Gaussian blur filter to detect only the grain boundaries (i.e., a filter for internal grain color changes). For each thin section, we selected a circular area of ~20 mm^2 (3000 pixels diameter) representative of the central part of each sample, to conduct the pore shape and distribution analysis (original thin section and zoomed area provided as supporting material).

EXPERIMENTAL RESULTS

The good linear correlations shown by V_P, $1/Q_P$ and resistivity (Figure 3), allow estimates of a missing property (among these three) in shallow sandy sedimentary formations, particularly interesting for seismic-CSEM surveys calibration (Han et al., 2011a). Further, the observed linear trend persists over the three stress-oriented scenarios, with very little slope variations from S-0 to S-45 and S-90 for any considered properties. This linearity extends to relationships between parameters from different orientations (see correlation matrix in Appendix A).

A slight deviation from linearity is identified for $1/Q_P$ data in S45 and S90, in the low stress domain (P_{diff} < 13 MPa). Because of the sensitivity of $1/Q_P$ to microcracks, this turning point indicates the crack closure is more significant for S-45 and S-90. Therefore, a priori, the rearrangement of the microstructure with stress, in each case, is similarly affecting the elastic and electrical properties of the rock at the sample scale, but differently enough to produce different attenuations. We further develop this idea in the following section, through a sample- and micro-scale stress-dependency anisotropy assessment.

ANISOTROPY ASSESSMENT

The experimental results are presented in Table 1. The rock is weakly anisotropic, as the anisotropy is below 20% (Thomsen, 1986), for all the measured parameters. On average, V_P is lower in the direction perpendicular to bedding, as expected (e.g., Thomsen, 1986; Wang, 2002; Martínez and Schmitt, 2013; Falcon-Suarez et al., 2017a), and increases very little from S-0 to S-45 (<0.5%), and by ~2% with respect to S-90. $1/Q_P$ increases from S-0 to S-90 up to 17%, which disagrees with previous experimental data in well-defined VTI media (e.g., Best et al., 2007; Chichinina et al., 2009). S-45 is slightly more resistive than S-90 (~1.5%) and S-0 (~4%). The resistivity varies within ~5% between the three samples. This very little variation could be related to the high porosity of the sample, which leads it to respond quasi-homogeneously to the electrical current propagation.

Elastic anisotropy

The three Thomsen's parameters for VTI media expressed for ultrasonic velocity show anisotropy below 4% (Figure 4a). This weak anisotropy and its slight variation with stress (ε is practically unaffected, while γ and δ oscillate within 2%;

Figure 4a) indicate a minor effect of the compliant porosity on the elastic anisotropy, which can be related to a low fraction (or absence) of microcracks above P_{diff} = 13 MPa. Among the three parameters, δ exhibits the largest anisotropy variability. Because δ is the only parameter related to the velocity at 45º with respect to the bedding plane, the sample S-45 might have experienced larger microstructural changes during the experiment than S-0 and S-90. Our elastic anisotropy values agree with those for poorly consolidated (saturated) sandstones reported by Thomsen (1986), the homogeneous Corvio sandstone in Falcon-Suarez et al. (2017a) above its crack closure stress limit, and the microcracks-free synthetic sandstone with penny shaped voids presented in Tillotson et al. (2014). By contrast, our results disagree with the data reported by Best et al. (2007) for water saturated sandstones partially damaged during core extraction (i.e., stress-release induced-microcracking).

Best et al. (2007) found complex relationships between P- and S-wave attenuation anisotropy parameters (ε_Q and γ_Q), the stress and the microstructure of the rock. The attenuation anisotropy of our rock is more significant than that estimated from the velocity. ε_Q exhibits largest attenuation anisotropy and lowest variation with pressure (~26 ± 3%), followed by δ_Q (~12 ± 4%) (Figure 4b). From expression 8, under constant saturation we expect changes in δ_Q associated with opening microcracks during unloading. However, among the three anisotropy attenuation parameters, δ_Q is the one showing less variation and dispersion. This observation suggests the microcracks closure stress limit of the rock (Falcon-Suarez et al., 2017a) is below P_{diff} = 13 MPa, supporting the turning point in the linear trends of $1/Q_P$ with V_P and resistivity for the low stress conditions (Figure 3). Also, γ_Q has

low anisotropy and large dispersion (γ_Q ~3 ± 8%), which has been previously related to layering effects in non-fractured sandstones (Tillotson et al., 2012).

With the anisotropy parameters, we obtained the (velocity and attenuation) VTI models for our rock. We observe mismatches between the modeling and experimental data (Figure 5), more significant for the attenuation, with respect to stress. The VTI model for ultrasonic velocity explains reasonably well the observations at high differential pressures but, when decreasing P_{diff} the model underestimates some of the observations at 45º. This effect is more significant for P_{diff} = 13 MPa, where the data points are horizontally shifted (denoted with λ in Figure 5) by up to 10º with respect to the theoretical predictions. This shift could be triggered by the minimum deviatoric stress applied (0.5 MPa), with stronger influence on grains rearrangement at low differential pressures. The S-45 attenuation anisotropy data points are also horizontally shifted with respect to the VTI modeling (Figure 5b). But, unlike the velocity, the largest discrepancy is associated with the first state of stress at the maximum compression (P_{diff} = 33 MPa), recovered with the stress decay. This evolution shows the stress history of the sample, with a first prompt consolidation with a poor grains arrangement, followed by a late consolidation with grain rearrangement during unloading. Hence, velocity is more conditioned by the grain-to-grain stress, while attenuation by the quality of the grain arrangement (i.e., presence of microcracks), which is more significant at oblique angles with respect to original layering.

Electrical anisotropy

Figure 6 shows both scale factor and stress dependency effects on the resistivity anisotropy. The scale effect is evident when comparing the magnitude of the resistivity anisotropy (bulk) factors between samples (λ_E and λ_e; Figure 6a) with

the individual (intrinsic) factors (λ_{E^*} and λ_{e^*}; Figure 6b) calculated from the three (orthogonal) principal electrical resistivity components ($R_1 > R_2 > R_3$) of each sample (obtained by applying the EHAR technique (North et al., 2013)); i.e., λ_E and λ_e are much lower than λ_{E^*} and λ_{e^*}. In general terms, the bulk resistivity decreases as S-45 > S-0 > S-90. The stress dependency of the bulk electrical anisotropy is therefore controlled by the rock fabric (layering), since λ_E increases with stress while λ_e remains constant. This finding is supported by λ_{E^*} and λ_{e^*}, which drop congruently with the decreasing stress for S-0, less slightly for S-45, and remain constant or even increase for S-90.

To further analyse the electrical heterogeneity and anisotropy of the rock, we display the three resistivity components of each core sample in a stereographic projection, considering both the differential and pore pressures (Figure 7).

The analysis shows the grains rearrangement induced by the first loading (test initiation) conditions the resistivity anisotropy, after which S-0 is the only sample with the expected orientation. The projection corroborates a congruent resistivity distribution for S-0 for the whole P_{diff} range, with maximum resistivity (R_1) along the vertical direction and two similar and horizontal low resistivity values (R_2 and R_3) representing the bedding plane. S-45 has a defined R_1 pseudo-perpendicular to its vertical axis, while R_2 and R_3 show pore pressure induced rotation with respect to R_1 at oblique angles, particularly at P_{diff} < 23 MPa. S-90 exhibits a more chaotic distribution of the three principal components, with an unclear rotation pattern of R_1 and R_2 with respect to R_3 due to the interplay between P_{diff} and P_p. This interplay is further analyzed below.

MICROMECHANICAL ASSESSMENT

Microstructural analysis

Previous experimental studies highlight the effect of the anisotropic intrinsic features of sandstones on the measured elastic and electrical properties (Han et al., 2011a, b; Falcon-Suarez et al., 2019). Here, the intrinsic resistivity anisotropy shows significant differences from one sample to another, supporting the idea that the microstructure conditions the stress-induced anisotropy development. Further, the ultrasonic properties show that while velocities (less sensitive to pore shape) are well explained by theoretical models, the attenuation data evidence some deviation at intermediate layering angles.

The thin sections extracted from the three samples post-testing reveal that, on a general basis, the grain distribution follows the fabric observed at hand-scale, in all cases (Figure 8). Our basic petrographic analysis agrees with the most complete description of the precursor YCIC sandstone formation reported in Scott et al. (2009). We identify a major granular framework composed of quartz and feldspar with minor phyllosilicates components (micas and clays), with iron-oxide cement and clay-size grains preferentially occupying the dark bands and interstitial pores. The clay minerals (illite) and iron-oxide cement bands are likely affecting the resistivity by increasing it due to clogging of the main fluid paths. Conversely, the clay minerals (illite) may also reduce resistivity by providing an extra conductive path – double layer (Han et al., 2011a). However, the low illite content (3%) together with the high porosity of the sample imply the role of the clay fraction is minor in our case.

S-45 shows evidences of grains rotation, exceeding the 45º angle orientation of the expected layering inclination. This observation explains the deviation of the measured data with respect to the elastic model at 45º (Figure 4), which is minor for

the V_P that barely depends on the pore shape (Han et al., 2011b), but significant for attenuation (Figure 5). Also, some mineral particles of S-45 show internal micro-cracks, probably linked to preferential grain-to-grain contacts orientations that favored local high stress development during the loading/unloading cycles. The stress-induced family of micro-cracks could have also contributed to increase the attenuation as the differential pressure was decreasing during the test. This stress-induced micro-cracking is less evident in S-0 and S-90, although the latter shows similar attenuation dispersion as S-45 at low differential stress (Figure 3). This disagreement suggests the stress-induced micro-cracking might have played a secondary role in our study.

For each sample, the orientation and length of major and minor axes of continuous grain edges were plotted as rose diagrams, equivalent to the pore shape elongation. To avoid detecting the edges of the thin sections as grain boundary orientation, rose diagrams were calculated on circular subareas of the same diameter acquired from each thin section. Hence, rose diagrams are not representative of the whole sample but of a specific location on the thin section. For the investigated area, the rose diagrams suggest the presence of different pore shapes in each sample. S-0 shows one predominant pore elongation along the horizontal plane (0º), and very little contribution to intermediate angles. Likewise, S-45 shows a marked oblique pore elongation (40 - 60º), but with more contribution of the intermediate elongations. Finally, S-90 exhibits a more homogeneous elongation orientation distribution. Although limited by the 2D nature of the thin section, we observe an increasing pore aspect ratio sequence as S-0 > S-45 > S-90. Accordingly, the observed weak electrical anisotropy can be mainly conditioned by the pore shape, in agreement with the observations in Nabawy et al. (2010) for high

porosity sandstones. More recently, Cilli and Chapman (2020) also demonstrate the influence of the pore shape on resistivity. Nevertheless, any comparison between thin sections and the observed results under confining stress must be understood in qualitative terms, since the stress conditions are different (i.e., experimental confining pressure versus atmospheric conditions).

In all cases, the results are consistent with the orientation of the main resistivity anisotropy components (Figure 7). The increasing dispersion from S-0 to S-90 might be related to heterogeneous distribution of the stress inside the sample (e.g., Dautriat et al., 2009; Yurikov et al., 2018). Yurikov et al. (2018) report results from numerical modeling (supported by ultrasonic data), which indicate the distribution of stress inside core plugs increases or decreases hyperbolically from the lateral sides to the center of the sample, depending on the elastic contrast between the sample and the axial confining platens. Also, according to their results, the lower the length-to-diameter ratio of the sample, the larger the heterogeneous stress distribution. In our case, the elastic contrast between the PEEK-buffer rods of our rig-platens and the poorly consolidated sandstone, together with the low length-to-diameter ratio of the samples, might have led to stress-induced grains rearrangement. This deformation pattern agrees with the hyperboloid-like shape observed on the three core plugs post-test (Figure 1b), and is particularly significant for S-90.

Stress dependency of elastic and electrical properties

We designed the stress sequence of the test to account for systematic changes in both the pore (P_p) and differential ($P_{diff} = P_c - P_p$) pressures, while keeping P_{diff} and P_p constant in each case. Thus, our data allow for an assessment of the differential effect of the confining and pore pressure on the measured parameters

through the effective stress coefficient n, that can be derived as follows (Todd and Simmons, 1972):

$$n_{(\beta)}=1-\frac{\left(\partial\beta/\partial P_p\right)_{P_{diff}}}{\left(\partial\beta/\partial P_{diff}\right)_{P_p}}, \qquad (20)$$

where β is any measured property of the sample. Once n is determined, differential pressure transforms into effective pressure as $P_{eff} = P_c - nP_p$.

Table 2 shows the effective stress coefficients for P-wave velocity (V_P) and attenuation ($1/Q_P$), and resistivity. The results represent the average of the four n-values computed from P_{diff} and P_p gradients of each P_p-stress path. Our results agree with previous experimental data on sandstones for V_P (e.g., Christensen and Wang, 1985; Prasad and Manghnani, 1997; Falcon-Suarez et al., 2019), and the scarce data reported in the literature and predictions for resistivity (Berryman, 1992; Falcon-Suarez et al., 2019); they are slightly higher (but with less dispersion) than those for $1/Q_P$ (Prasad and Manghnani, 1997; Falcon-Suarez et al., 2019).

In general, the n-values for each parameter show very little variation between samples. According to Glubokovskikh and Gurevich (2015), we can divide our parameters into scale-dependent (resistivity) and scale-independent (ultrasonic waves) properties. Only in the latter case we obtain $n = 1$ when the medium is homogeneous, isotropic and elastic, and under drainage conditions (Berryman, 1992; Glubokovskikh and Gurevich, 2015). However, the violation of at least one of the previous conditions led to an opposing response of P-waves in our case, being the confining stress dominant for velocity ($n < 1$) and the pore pressure for attenuation ($n > 1$). In other words, P-wave data can provide simultaneous information about the confining and pore pressure changes; we also observe that this double dependency is also slightly anisotropic (i.e., minimum for S-45 and

maximum for S-0; see Table 2). Han et al. (2011b) find that, for clean sandstones, the sensitivity of the attenuation to confining pressure increases with the aspect ratio of the open pores, while the contrary occurs for the resistivity. Evidence of grain rotation would lead to higher pore aspect ratios for S-45 than S-0 or S-90, at least locally, which is reflected in a lower *n*-value for attenuation.

Pore pressure is largely affecting the resistivity compared to the confining, with *n*-values above unity for the three samples. The resistivity *n*-value is anisotropic and linked to the bulk resistivity (i.e., S-45 > S-0 > S-90), because the higher the bulk resistivity, the lower the pore connectivity and likewise the effect of the pore fluid. This observation gains importance when resistivity anisotropy is used to estimate permeability anisotropy, which is essential in reservoir engineering to evaluate recovery rates (e.g., Dautriat et al., 2009) or the dynamics of the CO_2 plume advance during CO_2 storage. Furthermore, knowing the directions in which reservoirs are more affected by pore pressure changes could help improve numerical modeling for fractured reservoirs, particularly sensitive to injection activities (Jansen et al., 2019).

According to the results reported by Zisser and Nover (2009), for low porosity sandstones, and by Nabawy et al. (2010), for high porosity ones, the estimate of permeability from resistivity in variably stress conditions is only possible when the porosity is high enough for the main flow paths to remain active during compressive events (i.e., permeability remains unaffected by changes in the compliant porosity). We can analyze the differential effect of compressibility (i.e., changes in compliant and stiff porosity) on the elastic and electrical properties, using the following function (e.g., Eberhart-Phillips et al., 1989; Kaselow and Shapiro, 2004; Shapiro, 2003):

$$Y\left(P_{eff}\right) = A_Y + B_Y P_{eff} - C_Y \exp^{(-D_Y P_{eff})}, \qquad (21)$$

with *A*, *B*, *C* and *D* being the fitting parameters for the variable *Y*, equal to any elastic parameter considered, including P- and S-wave velocities and elastic moduli (Shapiro, 2003), under ideal hydrostatic loading conditions. Kaselow and Shapiro (2004) demonstrate that *D* is also valid for ($\log_{10}$) resistivity.

We used the equation 21 to fit our three parameters. Despite the universality of the parameter *D* is based on sample elasticity, homogeneity, isotropic stress-field or low porosity assumptions (Shapiro, 2003), we obtained close *D*-values for velocity and resistivity; but not for attenuation (Table 3). For each sample, the lower exponent of resistivity with respect to V_P and $1/Q_P$ adjustments indicate stress dependency of resistivity is more linear. In turn, this trend indicates resistivity is more sensitive to changes in stiff porosity, while ultrasonic (elastic) properties are preferentially affected by variations of the compliant porosity fraction (Kaselow and Shapiro, 2004). This behavior, together with the effective stress coefficient information, prove the potential of the elastic-electrical link to evaluate how injection/depletion mechanisms (i.e., pore pressure changes) affect the reservoir integrity, in agreement with Kaselow and Shapiro (2004).

More importantly, we observe the fitting parameters of the expression above are also reflecting anisotropy. The parameters *C* and *D* in the equation 21 provide useful information about the sensitivity and the rate of crack compliance with increasing stress, respectively (Eberhart-Phillips et al., 1989). Then, a priori, we could use parameters *C* and *D* to evaluate the stress dependency anisotropy of rocks. Thus, we observe the faster the cracks close (i.e., the higher *D* is) with P_{eff}, the lower the importance of the cracks (i.e., *C*) for any of the considered properties (i.e., *D* and *C* vary inversely). For S-0 and S-90 the cracks closure present similar values (except for $1/Q_P$), and occurs more rapidly than S-45. These results suggest

the porosity fraction related to cracks accommodate more rapidly and therefore has less importance on any measured property at oblique grains orientation angles with respect to the direction of the main stress components.

However, because we are violating some of the conditions for the universality of *D*, the adjustment of our three variables (V_P, $1/Q_P$ and resistivity) led to different fittings (Table 2). Therefore, we limit our analysis to compare same parameters between samples. Further investigation is required to determine intermediate values before developing a robust anisotropic stress dependency for the elastic and electrical properties of poorly consolidated sandstones.

DISCUSSION

Although weakly cemented, the rock remains weakly anisotropic under variable stress conditions because the stress dependency of the measured parameters is likewise anisotropic. Attenuation anisotropy (~20%) is much stronger than both velocity (~4%) and resistivity (<2%) anisotropies, and shows greater variations with pressure. Unlike attenuation, electrical resistivity anisotropy is relatively weak and hardly changes with pressure. If these pressure dependent anisotropies are due solely to the opening/closing of microcracks in response to pressure changes, symptomatic of a general geomechanical response of the rock, then we infer that attenuation anisotropy is the best guide to identify in situ fracture orientation and dilation.

We found strong linear correlations between velocity, resistivity and attenuation, for our range of differential pressures, at 0°, 45° and 90° to the (vertical) bedding normal for P-wave velocity and resistivity, while only at 0° for the attenuation. The correlations are statistically robust and potentially useful to infer one of the three parameters from another, whichever is available. But, even more, cross-

plotting any two parameters from any orientation lead to linear correlation coefficients (R^2) above 0.9 in all cases (see correlation matrix in Appendix B), allowing multi-parametric estimates of the rock anisotropy. Thereafter, a combined elastic-electrical anisotropy assessment could be used to identify flow (from electrical) and deformation patterns (from elastic) in reservoirs.

Assessing the elastic and electrical properties of reservoir rocks at the microscale is crucial to understand the stress-dependent geological processes, to properly develop predictive models and interpret the outcomes. For instance, Louis et al. (2003) remark the need to distinguish between voids and matrix related anisotropy (responsible of matrix permeability and internal deformation processes, respectively), before interpreting the fracture scale features. Farrell et al. (2014) find grain-scale deformation evidence from faulting system rocks, which explain anomalous large-scale preferential permeability (by an order of magnitude) in parallel than along the fault dip (i.e., along depositional lamination). Our results support the Farrell et al. (2014)'s interpretation. The highest resistivity value (equivalent to lowest permeability) in our experiment was obtained along the direction perpendicular to rock lamination on sample S-0 at the sample scale. However, when comparing bulk resistivity values, S-0 presented the lowest one. Therefore, our test highlights the importance of a good microscale anisotropy assessment to properly interpret the anisotropy of larger scales geological complexes, in agreement with previous works (e.g., Kaselow and Shapiro, 2004; Louis et al., 2004; Best et al., 2007; Wang et al., 2009; North et al., 2013; Farrell et al., 2014; North and Best, 2014; Falcon-Suarez et al., 2017a, c, 2019; Bayrakci et al., 2018; Han, 2018).

Grain orientation with respect to the principal stress field conditions grain-to-grain stress, which is directly conditioning the P-wave attributes (V_P and $1/Q_P$). Also, this grain-to-field stress orientation interplay indirectly influences the pore shape development during changes of the state of stress, eventually reflected in the electrical anisotropy (Nabawy et al. 2010; Cilli and Chapman, 2020). Our analysis of the stress dependency of anisotropy reveals that both the elastic and electrical properties respond differently to stress changes, depending on microcracks alignment with respect to the stress field. When oriented at oblique angles, crack closure with stress occurs more rapidly. Upscaling our results, we could expect sharp permeability variations with depth in dipping formations and more gradual in horizontal and vertical sedimentary strata. Changes in the state of stress due to either a variation of effective stress or the direction of the main components of stress, affect fracture distributions from the microstructure to large faulting systems. In turn, the anisotropy of the mechanical and transport properties of the rock formation are likewise affected.

This study considers laboratory grain scale (grain contact microcracks) and meso-scale (bedding plane) causes of geophysical anisotropy that could nevertheless affect macro-scale geophysical surveys by analogy. These effects can be up-scaled with knowledge of the underlying physical mechanisms related to micro-crack squirt flow (e.g., Dvorkin et al., 1995), ionic conductivity (e.g., Glover et al., 1994), and their respective elastic wave and electrical measurement frequency dependence (e.g., Dvorkin et al., 1995; Han et al., 2011a; North et al., 2013), including multiple layering effects (e.g., Backus, 1962; Sams et al., 1997). Then, this information can be used to validate coupled hydro-mechanical and seismic models, which improve the prediction of geomechanical manifestations in reservoirs (i.e.,

microseismicity), associated with subsidence in depleted reservoirs (Angus et al., 2015), ground-surface uplift and fracture creation/reactivation during CO_2 storage (Rutqvist, 2012; Jansen et al., 2019) and the evolution of preferential pathways for fluid migration through preexisting sub-vertical structures known as chimneys (Marín-Moreno et al., 2019).

CONCLUSIONS

In this first experiment focused on weakly cemented, poorly consolidated sandstone reservoirs, we show the potential of a combined assessment of the elastic and electrical anisotropies and their stress dependencies to improve the understanding of reservoirs subjected to human activities. The elastic (P-wave velocity and attenuation) and electrical (resistivity) anisotropies of weakly anisotropic poorly consolidated sandstones evolve similarly with stress. Strong linear correlations between the three parameters along the three considered directions (0º, 45º and 90º respect to the bedding plane of the rock) occur above a threshold stress, marked by the lack of linearity in the attenuation (more sensitive to cracks evolution), which suggests the porosity reduction rapidly overlaps the crack compliance effect. Above this crack-closure stress limit – the common state for real geological complexes, the joint elastic-electrical anisotropy framework of shallow sandstone reservoirs can be inferred from unidirectional measurements, provided that the rock bedding plane orientation is known.

The analysis of the microstructure and the stress-dependency of the three properties revealed that the sensitivity and celerity of crack closure are also anisotropic parameters. Resistivity is more sensitive to changes in stiff porosity, while elastic properties are preferentially affected by variations of the compliant porosity fraction. These sensitivities are anisotropic. The porosity fraction related to

cracks accommodate more rapidly and therefore has less importance on any measured property at oblique grains orientation angles with respect to the direction of the main stress components. The effective stress coefficient is also anisotropic for the three measured parameters. The resistivity and to a lesser extent attenuation are more sensitive to pore pressure changes, but less significantly at oblique angles. The velocity is slightly more affected by confining pressure variations, particularly at oblique angles. Combining this information, electrical anisotropy could be a useful indicator to estimate changes in the state of stress of reservoirs during production and injection activities.

APPENDIX A

CORRELATION MATRIX

Figure A-1 shows the correlations between the three measured parameters V_P, $1/Q_P$ and resistivity, for the three orientations of measurement (0°, 45° and 90º respect to the rock bedding). In all cases, the Pearson's correlation coefficient is above 0.9.

REFERENCES

Alemu, B. L., E. Aker, M. Soldal, Ø. Johnsen, and P. Aagaard, 2013, Effect of sub-core scale heterogeneities on acoustic and electrical properties of a reservoir rock: a CO_2 flooding experiment of brine saturated sandstone in a computed tomography scanner: Geophysical Prospecting, **61**, 235-250, doi: 10.1111/j.1365-2478.2012.01061.x

Angus, D. A., M. Dutko, T. G. Kristiansen, Q. J. Fisher, J. M. Kendall, A. F. Baird, J. P. Verdon, O. I. Barkved, J. Yu, and S. Zhao, 2015, Integrated hydro-mechanical and seismic modelling of the Valhall reservoir: A case study of predicting subsidence, AVOA and microseismicity: Geomechanics for Energy and the Environment, **2**, 32-44, doi: 10.1016/j.gete.2015.05.002.

Attias, E., K. Amalokwu, M. Watts, I. H. Falcon-Suarez, L. North, G. W. Hu, A. I. Best, K. Weitemeyer, and T. A. Minshull, 2020, Gas hydrate quantification at a pockmark offshore Norway from joint effective medium modelling of resistivity and seismic velocity: Marine and Petroleum Geology, **113**, 104151, doi:10.1016/j.marpetgeo.2019.104151.

Backus, G. E., 1962, Long-wave elastic anisotropy produced by horizontal layering: Journal of Geophysical Research (1896-1977), **67**, 4427-4440, doi:10.1029/JZ067i011p04427.

Bayrakci, G., I. H. Falcon-Suarez, T. A. Minshull, L. North, A. Barker, B. Zihlmann, S. Rouméjon, and A. I. Best, 2018, Anisotropic Physical Properties of Mafic and Ultramafic Rocks From an Oceanic Core Complex: Geochemistry, Geophysics, Geosystems, **19**, 4366– 4384, doi: 10.1029/2018GC007738.

Berryman, J. G., 1992, Effective stress for transport properties of inhomogeneous porous rock: Journal of Geophysical Research: Solid Earth, **97**, 17409-17424, doi: 10.1029/92JB01593.

Best, A. I., 1992, The prediction of the reservoir properties of sedimentary rocks from seismic measurements, University of Reading.

Best, A. I., J. Sothcott, and C. McCann, 2007, A laboratory study of seismic velocity and attenuation anisotropy in near-surface sedimentary rocks: Geophysical Prospecting, **55**, 609-625, doi: 10.1111/j.1365-2478.2007.00642.x.

Carcione, J. M., B. Ursin, and J. I. Nordskag, 2007, Cross-property relations between electrical conductivity and the seismic velocity of rocks: Geophysics, **72**, no. 5, E193-E204, doi: 10.1190/1.2762224.

Chichinina, T., I. Obolentseva, L. Gik, B. Bobrov, and G. Ronquillo-Jarillo, 2009, Attenuation anisotropy in the linear-slip model: Interpretation of physical modeling data: Geophysics, **74**, no. 5, WB165-WB176, doi: 10.1190/1.3173806.

Christensen, N. I., and H. F. Wang, 1985, The Influence of pore pressure and confining pressure on dynamic elastic properties of Berea sandstone: Geophysics, **50**, no. 2, 207-213, doi: 10.1190/1.1441910.

Cilli, P. A., and M. Chapman, 2020, The power-law relation between inclusion aspect ratio and porosity: Implications for electrical and elastic modeling: Journal of Geophysical Research: Solid Earth, e2019JB019187, doi:10.1029/2019jb019187.

Dautriat, J., N. Gland, J. Guelard, A. Dimanov, and J. Raphanel, 2009, Axial and Radial Permeability Evolutions of Compressed Sandstones: End Effects and Shear-band Induced Permeability Anisotropy: Pure and Applied Geophysics, **166**, 1037-1061, doi: 10.1007/s00024-009-0495-0.

Dvorkin, J., G. Mavko, and A. Nur, 1995, Squirt flow in fully saturated rocks: Geophysics, no. 1, **60**, 97-107, doi: 10.1190/1.1443767.

Eberhart-Phillips, D., D.-H. Han, and M. D. Zoback, 1989, Empirical relationships among seismic velocity, effective pressure, porosity, and clay content in sandstone: Geophysics, **54**, no. 1, 82-89, doi: 10.1190/1.1442580.

Falcon-Suarez, I., L. North, K. Amalokwu, and A. Best, 2016, Integrated geophysical and hydromechanical assessment for CO_2 storage: shallow low permeable reservoir sandstones: Geophysical Prospecting, **64**, 828-847, doi: 10.1111/1365-2478.12396.

Falcon-Suarez, I., J. Canal-Vila, J. Delgado-Martin, L. North, and A. Best, 2017a, Characterisation and multifaceted anisotropy assessment of Corvio sandstone for geological CO_2 storage studies: Geophysical Prospecting, **65**, 1293-1311, doi: 10.1111/1365-2478.12469.

Falcon-Suarez, I., G. Papageorgiou, A. Chadwick, L. North, A. Best, and M. Chapman, 2018, CO_2-brine flow-through on an Utsira Sand core sample: Experimental and modelling. Implications for the Sleipner storage field: International Journal of Greenhouse Gas Control, **68**, 236-246, doi: 10.1016/j.ijggc.2017.11.019.

Falcon-Suarez, I., H. Marín-Moreno, F. Browning, A. Lichtschlag, K. Robert, L. J. North, and A. I. Best, 2017b, Experimental assessment of pore fluid distribution and geomechanical changes in saline sandstone reservoirs during and after CO_2 injection: International Journal of Greenhouse Gas Control, **63**, 356-369, doi: 10.1016/j.ijggc.2017.06.019.

Falcon-Suarez, I., G. Bayrakci, T. A. Minshull, N. J.L., A. I. Best, S. Rouméjon, and IODP-Expedition-357-Science-Party, 2017c, Elastic and electrical properties and

permeability of serpentinites from Atlantis Massif, Mid-Atlantic Ridge: Geophysical Journal International, **211**, 708–721, doi: 10.1093/gji/ggx341.

Falcon-Suarez, I. H., K. Amalokwu, J. Delgado-Martin, B. Callow, K. Robert, L. North, S. K. Sahoo, and A. I. Best, 2019, Comparison of stress-dependent geophysical, hydraulic and mechanical properties of synthetic and natural sandstones for reservoir characterization and monitoring studies: Geophysical Prospecting, **67**, 784-803, doi: 10.1111/1365-2478.12699.

Farrell, N. J. C., D. Healy, and C. W. Taylor, 2014, Anisotropy of permeability in faulted porous sandstones: Journal of Structural Geology, **63**, 50-67, doi: 10.1016/j.jsg.2014.02.008.

Glover, P. W. J., P. G. Meredith, P. R. Sammonds, and S. A. F. Murrell, 1994, Ionic surface electrical conductivity in sandstone: Journal of Geophysical Research: Solid Earth, **99**, 21635-21650, doi: 10.1029/94jb01474.

Glubokovskikh, S., and B. Gurevich, 2015, Effect of micro-inhomogeneity on the effective stress coefficients and undrained bulk modulus of a poroelastic medium: a double spherical shell model: Geophysical Prospecting, **63**, 656-668, doi: 10.1111/1365-2478.12222.

Guo, X., T. Yoshino, and I. Katayama, 2011, Electrical conductivity anisotropy of deformed talc rocks and serpentinites at 3 GPa: Physics of The Earth and Planetary Interiors, **188**, 69-81, doi: 10.1016/j.pepi.2011.06.012.

Han, T., 2018, Joint Elastic-Electrical Properties of Artificial Porous Sandstone With Aligned Fractures: Geophysical Research Letters, **45**, 3051-3058, doi: 10.1002/2018GL077541.

Han, T., A. I. Best, J. Sothcott, and L. M. MacGregor, 2011a, Joint elastic-electrical properties of reservoir sandstones and their relationships with

petrophysical parameters: Geophysical Prospecting, **59**, 518-535, doi: 10.1111/j.1365-2478.2010.00940.x.

Han, T., A. I. Best, J. Sothcott, and L. M. MacGregor, 2011b, Pressure effects on the joint elastic-electrical properties of reservoir sandstones: Geophysical Prospecting, **59**, 506-517, doi: 10.1111/j.1365-2478.2010.00939.x.

Jansen, J. D., P. Singhal, and F. C. Vossepoel, 2019, Insights From Closed-Form Expressions for Injection- and Production-Induced Stresses in Displaced Faults: Journal of Geophysical Research: Solid Earth, **124**, 7193– 7212, doi: 10.1029/2019jb017932.

Kaselow, A., and S. A. Shapiro, 2004, Stress sensitivity of elastic moduli and electrical resistivity in porous rocks: Journal of Geophysics and Engineering, **1**, 1-11, doi: 10.1088/1742-2132/1/1/001.

Kovalyshen, Y., J. Sarout, and M. Lebedev, 2018, On the interpretation of ultrasonic laboratory measurements in anisotropic media: Geophysics, **83**, C173-C178, no. 4, doi: 10.1190/geo2017-0634.1.

Kylander, O. S., and K. Kylander, 1999, Gimp the Official Handbook with Cdrom: Coriolis Value.

Lakio, S., J. Heinämäki, and J. Yliruusi, 2010, Colorful Drying: An Official Journal of the American Association of Pharmaceutical Scientists, **11**, 46-53, doi: 10.1208/s12249-009-9351-x.

Louis, L., C. David, and P. Robion, 2003, Comparison of the anisotropic behaviour of undeformed sandstones under dry and saturated conditions: Tectonophysics, **370**, 193-212, doi: 10.1016/S0040-1951(03)00186-0 .

Louis, L., P. Robion, and C. David, 2004, A single method for the inversion of anisotropic data sets with application to structural studies: Journal of Structural Geology, **26**, 2065-2072, doi: 10.1016/j.jsg.2004.03.005.

Marín-Moreno, H., Bull, J.M., Matter, J.M., Sanderson, D.J. & Roche, B.J., 2019. Reactive transport modelling insights into CO2 migration through sub-vertical fluid flow structures, International Journal of Greenhouse Gas Control, **86**, 82-92, doi: 10.1016/j.ijggc.2019.04.018.

Martínez, J. M., and D. R. Schmitt, 2013, Anisotropic elastic moduli of carbonates and evaporites from the Weyburn-Midale reservoir and seal rocks: Geophysical Prospecting, **61**, 363-379, doi: 10.1111/1365-2478.12032.

Nabawy, B. S., P. Rochette, and Y. Géraud, 2010, Electric pore fabric of the Nubia sandstones in south Egypt: characterization and modelling: Geophysical Journal International, **183**, 681-694, doi: 10.1111/j.1365-246X.2010.04789.x.

Nooraiepour, M., B. Bohloli, J. Park, G. Sauvin, E. Skurtveit, and N. H. Mondol, 2018, Effect of brine-CO_2 fracture flow on velocity and electrical resistivity of naturally fractured tight sandstones: Geophysics, **83**, no. 1, WA37-WA48, doi: 10.1190/geo2017-0077.1.

North, L., A. I. Best, J. Sothcott, and L. MacGregor, 2013, Laboratory determination of the full electrical resistivity tensor of heterogeneous carbonate rocks at elevated pressures: Geophysical Prospecting, **61**, 458-470, doi: 10.1111/j.1365-2478.2012.01113.x.

North, L. J., and A. I. Best, 2014, Anomalous electrical resistivity anisotropy in clean reservoir sandstones: Geophysical Prospecting, **62**, 1315-1326, doi: 10.1111/1365-2478.12183.

Prasad, M., and M. H. Manghnani, 1997, Effects of pore and differential pressure on compressional wave velocity and quality factor in Berea and Michigan sandstones: Geophysics, **62**, 1163-1176, doi: 10.1190/1.1444217.

Rathore, J. S., E. Fjaer, R. M. Holt, and L. Renlie, 1995, P- and S-wave anisotropy of a synthetic sandstone with controlled crack geometry: Geophysical Prospecting, **43**, 711-728, doi: 10.1111/j.1365-2478.1995.tb00276.x.

Rutqvist, J., 2012, The geomechanics of CO_2 storage in deep sedimentary formations: Geotechnical and Geological Engineering, **30**, 525-551, doi: 10.1007/s10706-011-9491-0.

Sahoo, S. K., B. N. Madhusudhan, H. Marín-Moreno, L. J. North, S. Ahmed, I. H. Falcon-Suarez, T. A. Minshull, and A. I. Best, 2018, Laboratory Insights Into the Effect of Sediment-Hosted Methane Hydrate Morphology on Elastic Wave Velocity From Time-Lapse 4-D Synchrotron X-Ray Computed Tomography: Geochemistry, Geophysics, Geosystems, **19**, 4502– 4521,doi: 10.1029/2018GC007710.

Sams, M. S., J. P. Neep, M. H. Worthington, and M. S. King, 1997, The measurement of velocity dispersion and frequency-dependent intrinsic attenuation in sedimentary rocks: Geophysics, **62**, 1456-1464, doi: 10.1190/1.1444249.

Scott, A., M. Vigorito, and A. Hurst, 2009, The Process of Sand Injection: Internal Structures and Relationships with Host Strata (Yellowbank Creek Injectite Complex, California, U.S.A.): Journal of Sedimentary Research, **79**, 568-583, doi: 10.2110/jsr.2009.062.

Shapiro, S. A., 2003, Elastic piezosensitivity of porous and fractured rocks: Geophysics, **68**, 482-486, doi: 10.1190/1.1567215.

Shapiro, S.A., Khizhniak, G.P., Plotnikov, V.V., Niemann, R., Ilyushin, P.Y. & Galkin, S.V., 2015. Permeability dependency on stiff and compliant porosities: a

model and some experimental examples, Journal of Geophysics and Engineering, **12**, 376-385, doi: 10.1088/1742-2132/12/3/376.

Thomsen, L., 1986, Weak elastic anisotropy: Geophysics, **51**, 1954-1966, doi: 10.1190/1.1442051.

Tillotson, P., J. Sothcott, A. I. Best, M. Chapman, and X.-Y. Li, 2012, Experimental verification of the fracture density and shear-wave splitting relationship using synthetic silica cemented sandstones with a controlled fracture geometry: Geophysical Prospecting, **60**, 516-525, doi: 10.1111/j.1365-2478.2011.01021.x.

Tillotson, P., M. Chapman, J. Sothcott, A. I. Best, and X.-Y. Li, 2014, Pore fluid viscosity effects on P- and S-wave anisotropy in synthetic silica-cemented sandstone with aligned fractures: Geophysical Prospecting, **62**, 1238-1252, doi: 10.1111/1365-2478.12194.

Todd, T., and G. Simmons, 1972, Effect of pore pressure on the velocity of compressional waves in low-porosity rocks: Journal of Geophysical Research, **77**, 3731-3743, doi: 10.1029/JB077i020p03731.

Wang, Z., 2002, Seismic anisotropy in sedimentary rocks, part 1: A single-plug laboratory method: Geophysics, **67**, 1415-1422, doi: 10.1190/1.1512787.

Wang, Z., and L.-J. Gelius, 2010, Electric and elastic properties of rock samples: a unified measurement approach: Petroleum Geoscience, **16**, 171-183, doi: 10.1144/1354-079309-013.

Wang, Z., L.-J. Gelius, and F.-N. Kong, 2009, Simultaneous core sample measurements of elastic properties and resistivity at reservoir conditions employing a modified triaxial cell – a feasibility study: Geophysical Prospecting, **57**, 1009-1026, doi: 10.1111/j.1365-2478.2009.00792.x.

Yurikov, A., M. Lebedev, and M. Pervukhina, 2018, Ultrasonic velocity measurements on thin rock samples: Experiment and numerical modeling: Geophysics, **83**, no. 2, MR47-MR56, doi: 10.1190/geo2016-0685.1.

Zhu, Y., and I. Tsvankin, 2006, Plane-wave propagation in attenuative transversely isotropic media: Geophysics, **71**, no. 2, T17-T30, doi: 10.1190/1.2187792 .

Zisser, N., and G. Nover, 2009, Anisotropy of permeability and complex resistivity of tight sandstones subjected to hydrostatic pressure: Journal of Applied Geophysics, **68**, 356-370, doi: 10.1016/j.jappgeo.2009.02.010.

FIGURE CAPTIONS

Figure 1. (a) Samples orientation with respect to the precursor YCIC sandstone block and orientation of the thin sections (T_0, T_{45} and T_{90}) post-mortem. (b) Core samples after the test.

Figure 2. Experimental rig.

Figure 3. Correlations between measured properties (P-wave velocity, V_P, attenuation, $1/Q_P$, and resistivity), considering all the state of stress adopted during the test: (a) V_P versus resistivity, (b) V_P versus $1/Q_P$, and (c) $1/Q_P$ versus resistivity. The four stress cycles are identified according to their pore pressure (P_p). Black, red and blue colors are used for samples S-0, S-45 and S-90, respectively. Deviation of $1/Q_P$ from linearity below P_{diff} = 13 MPa is marked.

Figure 4. (a) Velocity and (b) attenuation anisotropy parameters expressed as percentages of the three Thomsen's parameters (Thomsen, 1986) for transverse isotropy with a vertical axis of rotational symmetry (TIV).

Figure 5. Experimental data (points) for (a) P-wave velocity, V_P, and (b) attenuation, $1/Q_P$, the best fitting (dashed line) using a least square numerical regression, and the modeling results (solid lines) for each state of stress by substituting each set of Thomsen's parameters (derived from the elastic constants for velocities and attenuation; Table 1) in equations 17 and 18, respectively. The curves are labelled according to the pore pressure (P_p), while symbol size represents differential pressure (P_{diff}). The parameter λ indicates the misfit between the observed data and the modeling results. To facilitate the visualization, the unloading data is not displayed.

Figure 6. Resistivity anisotropy assessment using the maximum (λ_E, empty symbols) and intermediate (λ_e, solid symbols) resistivity anisotropy factors, through (a) the

magnitude of the anisotropy derived from the bulk resistivity between samples, and (b) within each sample after EHAR (subscript * for intrinsic resistivity; see text for details).

Figure 7. Stereographic plot illustrating the magnitude and orientation of the principle components (R_1, R_2 and R_3) of the tensorial anisotropy resistivity with respect to the vertical axis (center of the circumference, which represents the polar axis of the bedding plane) for the three samples (a) S-0, (b) S-45 and (c) S-90 (inversion scheme from North et al. 2013). Symbols represent pore pressure (P_p), and their size give the differential pressure (P_{diff}).

Figure 8. Microstructural analysis for the three samples (a) S-0, (b) S-45 and (c) S-90. At the top, zoomed areas of the thin sections with evidences of albite (Alb), quartz (Q) and illite (Ill). At the bottom, rose diagrams of grain boundary orientations obtained with image processing (edge detection) of vertical thin sections orientation. The edge detection analysis was performed on a 20 mm^2 circular area (3000 pixels diameter; see in supporting material) of each thin section, corresponding to the central part of each sample.

TABLE CAPTIONS

Table 1. Experimental results

Table 2. Effective stress coefficients ($n_{(\beta)}$) for the measured parameters (β)

Table 3. Fitting parameters of equation (20) for the elastic (V_P and $1/Q_P$) and electrical (resistivity) properties of the three samples (S-0, S-45 and S-90)

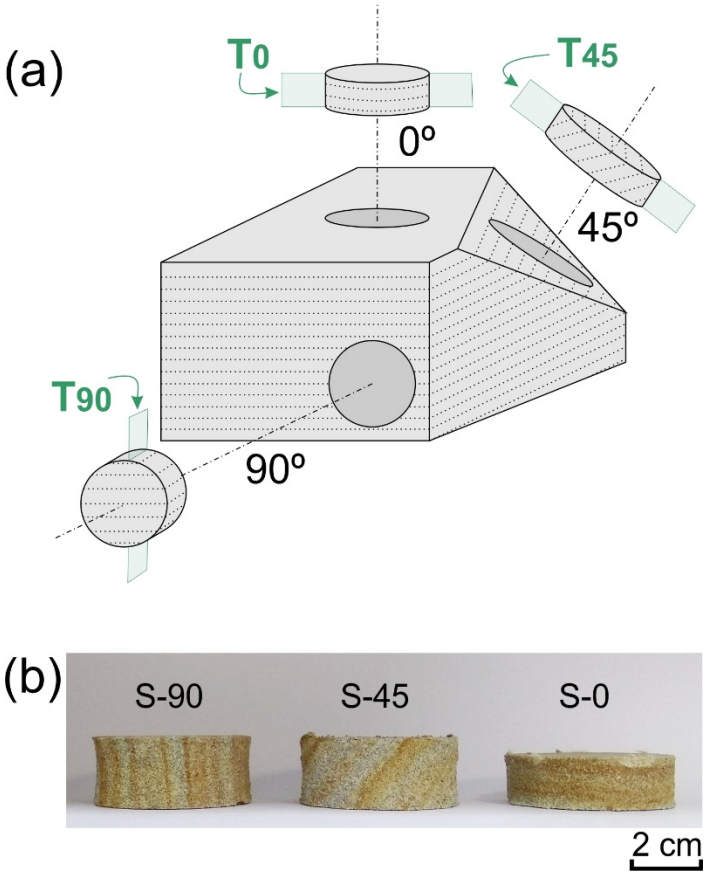

Figure 1. (a) Samples orientation with respect to the precursor YCIC sandstone block and orientation of the thin sections (T_0, T_{45} and T_{90}) post-mortem. (b) Core samples after the test.

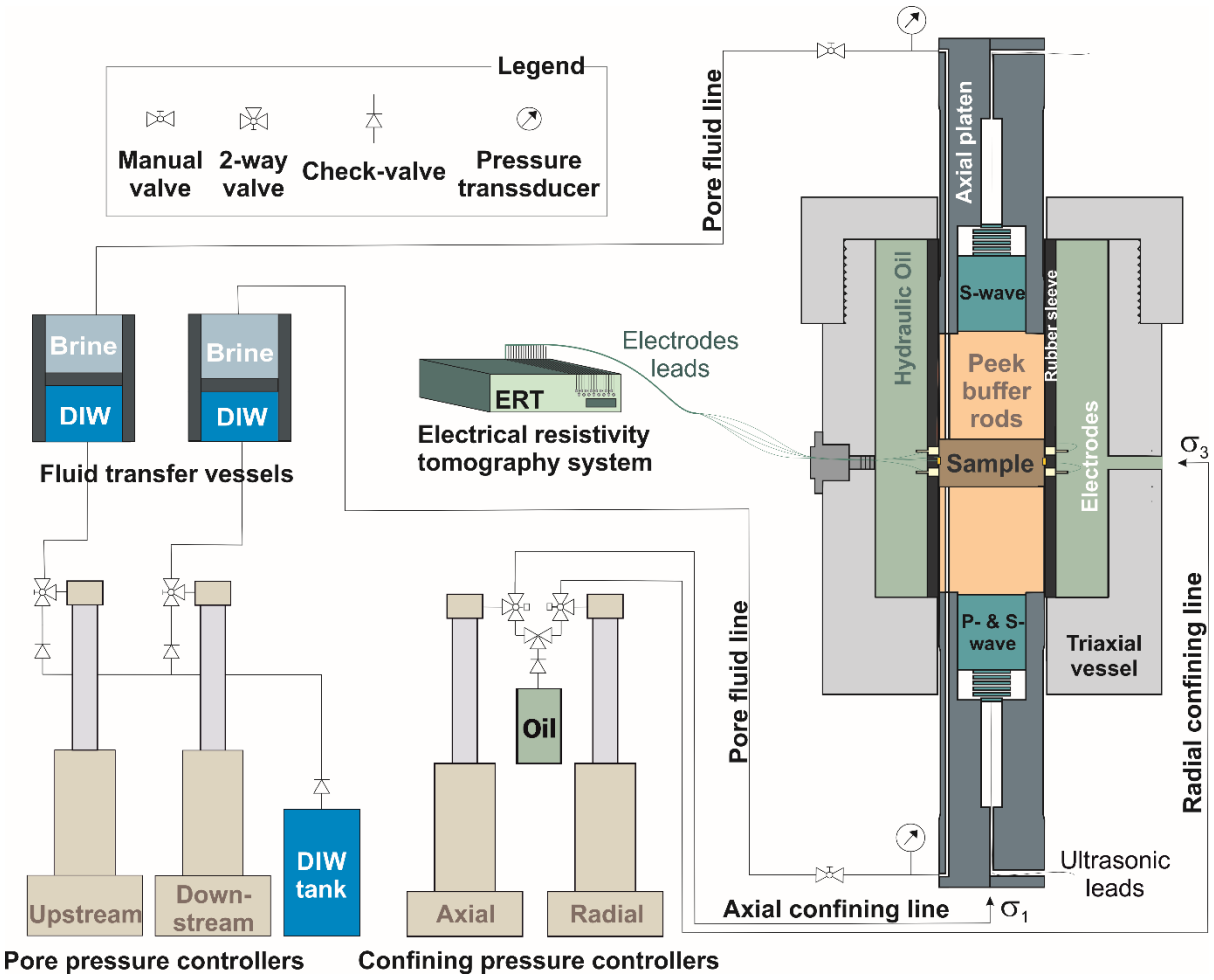

Figure 2. Experimental rig.

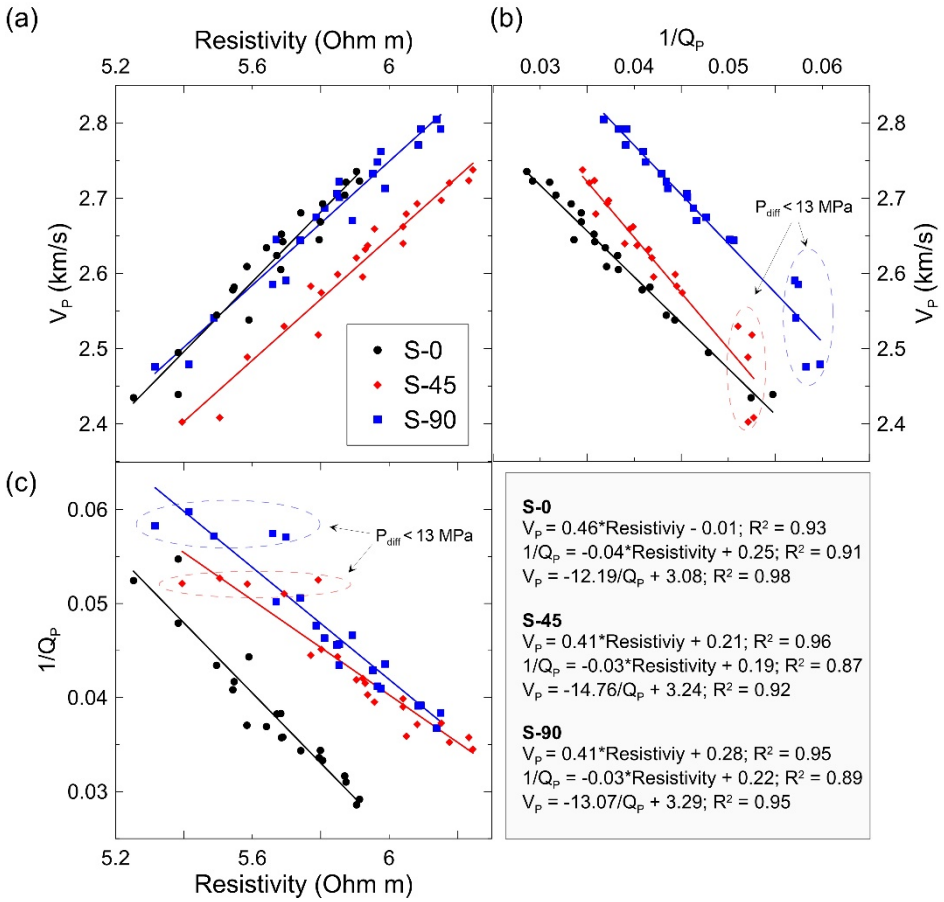

Figure 3. Correlations between measured properties (P-wave velocity, V_P, attenuation, $1/Q_P$, and resistivity), considering all the state of stress adopted during the test: (a) V_P versus resistivity, (b) V_P versus $1/Q_P$, and (c) $1/Q_P$ versus resistivity. The four stress cycles are identified according to their pore pressure (P_p). Black, red and blue colors are used for samples S-0, S-45 and S-90, respectively. Deviation of $1/Q_P$ from linearity below P_{diff} = 13 MPa is marked.

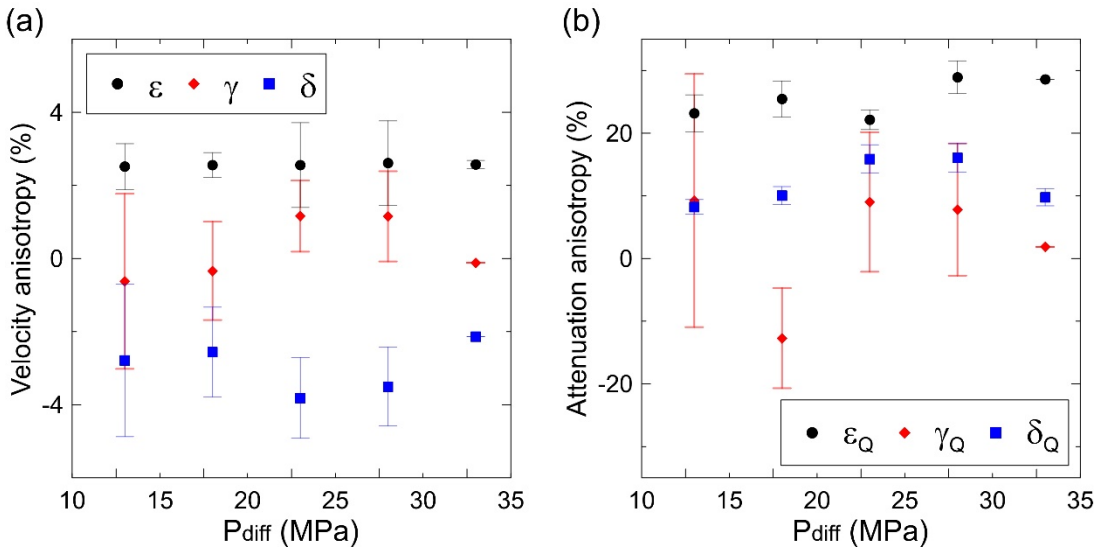

Figure 4. (a) Velocity and (b) attenuation anisotropy parameters expressed as percentages of the three Thomsen's parameters (Thomsen, 1986) for transverse isotropy with a vertical axis of rotational symmetry (TIV).

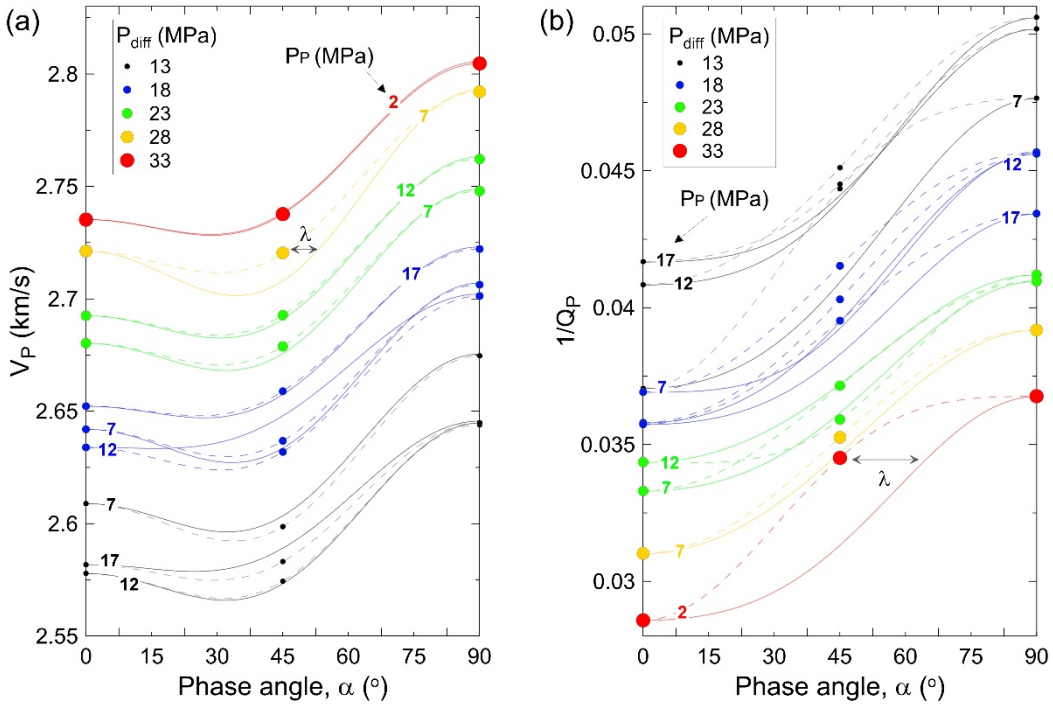

Figure 5. Experimental data (points) for (a) P-wave velocity, V_P, and (b) attenuation, $1/Q_P$, the best fitting (dashed line) using a least square numerical regression, and the modeling results (solid lines) for each state of stress by substituting each set of Thomsen's parameters (derived from the elastic constants for velocities and attenuation; Table 1) in equations 17 and 18, respectively. The curves are labelled according to the pore pressure (P_p), while symbol size represents differential pressure (P_{diff}). The parameter λ indicates the misfit between the observed data and the modeling results. To facilitate the visualization, the unloading data is not displayed.

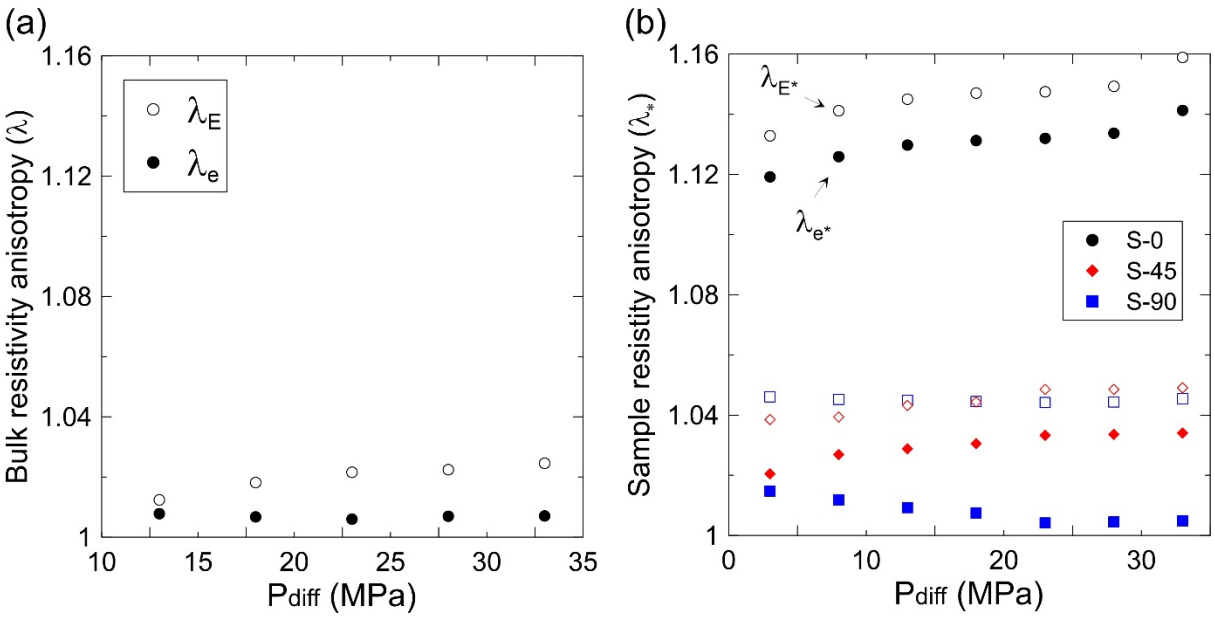

Figure 6. Resistivity anisotropy assessment using the maximum (λ_E, empty symbols) and intermediate (λ_e, solid symbols) resistivity anisotropy factors, through (a) the magnitude of the anisotropy derived from the bulk resistivity between samples, and (b) within each sample after EHAR (subscript * for intrinsic resistivity; see text for details).

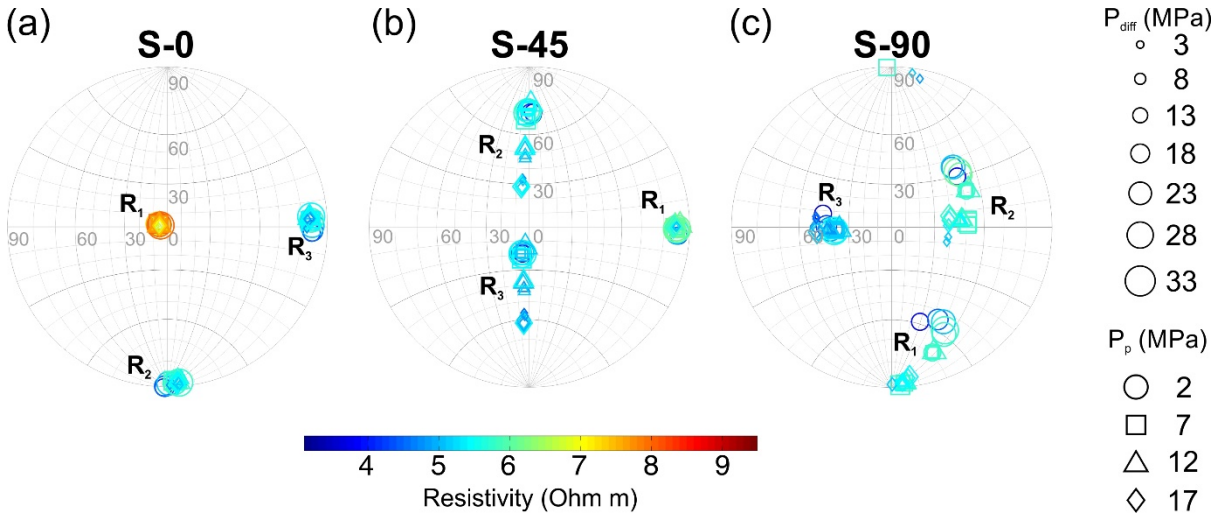

Figure 7. Stereographic plot illustrating the magnitude and orientation of the principle components (R_1, R_2 and R_3) of the tensorial anisotropy resistivity with respect to the vertical axis (center of the circumference, which represents the polar axis of the bedding plane) for the three samples (a) S-0, (b) S-45 and (c) S-90 (inversion scheme from North et al. 2013). Symbols represent pore pressure (P_p), and their size give the differential pressure (P_{diff}).

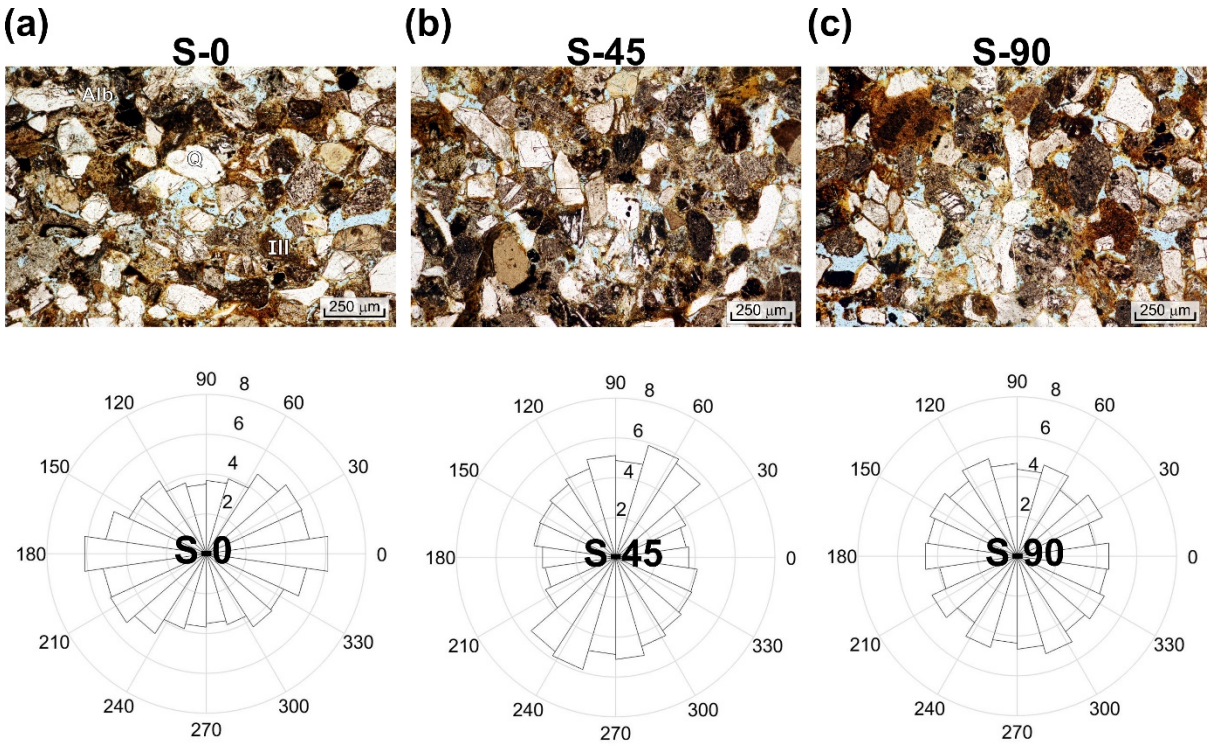

Figure 8. Microstructural analysis for the three samples (a) S-0, (b) S-45 and (c) S-90. At the top, zoomed areas of the thin sections with evidences of albite (Alb), quartz (Q) and illite (Ill). At the bottom, rose diagrams of grain boundary orientations obtained with image processing (edge detection) of vertical thin sections orientation. The edge detection analysis was performed on a 20 mm^2 circular area (3000 pixels diameter; see in supporting material) of each thin section, corresponding to the central part of each sample.